Neuro-Oncology
20(11), 1536–1546, 2018 | doi:10.1093/neuonc/noy066 | Advance Access date 28 April 2018

Intratumoral heterogeneity of oxygen metabolism and neovascularization uncovers 2 survival-relevant subgroups of IDH1 wild-type glioblastoma

Andreas Stadlbauer, Max Zimmermann, Arnd Doerfler, Stefan Oberndorfer, Michael Buchfelder, Roland Coras, Melitta Kitzwögerer, and Karl Roessler

Department of Neurosurgery, University of Erlangen-Nürnberg, Erlangen, Germany (A.S., M.Z., M.B., K.R.); Institute of Medical Radiology, University Clinic of St Pölten, St Pölten, Austria (A.S.); Department of Neuroradiology, University of Erlangen-Nürnberg, Erlangen, Germany (A.D.); Department of Neurology, University Clinic of St Pölten, St Pölten, Austria (S.O.); Department of Neuropathology, University of Erlangen-Nürnberg, Erlangen, Germany (R.C.); Department of Pathology, University Clinic of St Pölten, St Pölten, Austria (M.K.)

Corresponding Author: Prof. Dr. Andreas Stadlbauer, Department of Neurosurgery, University of Erlangen-Nürnberg, Schwabachanlage 6, 91054 Erlangen, Germany (andi@nmr.at).

Abstract

Background. The intratumoral heterogeneity of oxygen metabolism in combination with variable patterns of neovascularization (NV) as well as reprogramming of energy metabolism affects the landscape of tumor microenvironments (TMEs) in glioblastoma. Knowledge of the hypoxic and perivascular niches within the TME is essential for understanding treatment failure.

Methods. Fifty-two patients with untreated glioblastoma (isocitrate dehydrogenase 1 wild type [IDH1wt]) were examined with a physiological MRI protocol including a multiparametric quantitative blood oxygen level dependent (qBOLD) approach and vascular architecture mapping (VAM). Imaging biomarker information about oxygen metabolism (mitochondrial oxygen tension) and neovascularization (microvascular density and type) were fused for classification of 6 different TMEs: necrosis, hypoxia with/without neovascularization, oxidative phosphorylation (OxPhos), and glycolysis with/without neovascularization. Association of the different TME volume fractions with progression-free survival (PFS) was assessed using Kaplan–Meier analysis and Cox proportional hazards models.

Results. A common spatial structure of TMEs was detected: central necrosis surrounded by tumor hypoxia (with defective and functional neovasculature) and different TMEs with a predominance of OxPhos and glycolysis for energy production, respectively. The percentage of the different TMEs on the total tumor volume uncovered 2 clearly different subtypes of glioblastoma IDH1wt: a glycolytic dominated phenotype with predominantly functional neovasculature and a necrotic/hypoxic dominated phenotype with approximately 50% of defective neovasculature. Patients with a necrotic/hypoxic dominated phenotype showed significantly shorter PFS ($P = 0.035$).

Conclusions. Our non-invasive mapping approach allows for classification of the TME and detection of tumor-supportive niches in glioblastoma which may be helpful for both clinical patient management and research.

Key words

glioblastoma | mitochondrial oxygen tension | intratumoral heterogeneity | neovascularization | Warburg effect

Glioblastoma is the most common and malignant primary brain tumor, characterized by highly aggressive-invasive growth and resistance to therapy. Typically, radiological recurrence and clinical relapse occurs 6–7 months after surgery,[1] resulting in a median survival of only 14–16 months despite the best available treatments.[2,3] Accumulating evidence suggests that intratumoral heterogeneity and divergent development of subpopulations of

Importance of the study

The dismal prognosis of glioblastoma is largely attributed to the heterogeneous nature of the tumor, which is influenced by hypoxic and perivascular niches in the TME. Therefore, oxygen metabolism and neovascularization have the potential as a key biomarker for elucidation of pathophysiological mechanisms including therapy resistance and recurrence. Most of the available techniques, however, are not well suited for noninvasive in vivo characterization in humans. In this study, we used MRI biomarkers of oxygen metabolism and neovascularization in combination with an automatic classification strategy for non-invasive localization of hypoxic and vascular niches within the heterogeneously structured TME. Correlation with the dominating metabolic strategy for energy production uncovered 2 different metabolic phenotypes for newly diagnosed glioblastoma IDH1wt: a glycolytic phenotype with stable functional neovasculature, and a necrotic/hypoxic phenotype with high proportion of unstable defective dysfunctional neovasculature and a more aggressive tumor behavior. The glycolytic phenotype showed longer PFS.

cancer cells within the same tumor are probably the keys for understanding treatment failure.[4–6] Specific histopathological features, including pseudopalisading necrosis and microvascular proliferation, make glioblastoma one of the most hypoxic and vascularized of all solid tumors.[7] These microanatomical compartments present specific niches within the tumor microenvironment (TME) that regulate metabolic needs, immune surveillance, survival, invasion, and glioma stemlike cell maintenance.[7] The TME is emerging as a critical regulator of cancer progression and therapeutic response in primary and metastatic brain malignancies.[8] The dismal prognosis of glioblastoma is largely attributed to the heterogeneous nature of the tumor, which in addition to intrinsic molecular and genetic changes is also influenced by specialized TME niches in which the glioma cells reside.[9] In glioblastoma, 3 morphologically and functionally specialized tumor niches were described, including the vasculature as an integral regulatory part: (i) the perivascular, (ii) the hypoxic, and (iii) the vascular-invasive niches.[7] The perivascular and hypoxic niches are found within the tumor bulk and reside in the tumor neovasculature and the necrotic/hypoxic tumor regions, respectively.[7,10] In the vascular-invasive tumor niche, however, tumor cells co-opt normal blood vessels, enabling migration deep into the brain parenchyma.[11]

Besides the intratumoral heterogeneity in extent and degree of necrosis/hypoxia in combination with variable patterns of neovascularization, reprogramming of energy metabolism additionally influences the landscape of TME and represents a considerable problem in therapeutic management of glioblastoma.[12] In contrast to normal differentiated cells, which rely primarily on mitochondrial oxidative phosphorylation (OxPhos) to generate the energy needed for cellular processes, most cancer cells instead rely on aerobic glycolysis, a phenomenon termed the "Warburg effect." Aerobic glycolysis is an inefficient but faster way to generate adenosine 5′-triphosphate (ATP). However, the advantage it confers to cancer cells is not fully understood but the subject of intense research.[13]

The interplay between oxygen metabolism and neovascularization as well as the metabolic pathways for energy production are of crucial importance in tumor biology. Therefore, they have the potential as a key imaging biomarker for elucidation of pathophysiological mechanisms, including therapy resistance and recurrence. Most of the available techniques, however, are not well suited for in vivo characterization in humans due to their invasiveness (electrodes), limited availability and high costs (PET), or low spatial resolution (near-infrared spectroscopy). A novel MRI-based multiparametric approach has been recently proposed to obtain quantitative information about oxygenation metabolism and neovascularization in glioma patients.[14–18]

In this study, we built on this physiological MRI approach and hypothesized that fusion of imaging biomarker information about oxygen metabolism and neovascularization in combination with an automatic user-independent classification strategy provides more precise insights into the intratumoral heterogeneity of human glioblastoma's pathophysiology. We termed our approach TME mapping. The aim of our study was threefold: (i) non-invasive detection and investigation of hypoxic and vascular niches in the TME; (ii) correlation of TME niches with the dominating metabolic strategy for energy production to identify patient subgroups with newly diagnosed glioblastoma; and (iii) investigation of the relationship to clinical outcome.

Materials and Methods

Patients

The institutional review board approved this retrospective study. Written consent was obtained from all enrolled patients. A consecutively and prospectively populated institutional database was searched for patients with newly diagnosed untreated glioblastoma (World Health Organization [WHO] grade IV) between July 2015 and April 2017. Inclusion criteria were as follows: (i) age ≥18 years; (ii) MR scans using our study MRI protocol; (iii) pathologically confirmed glioblastoma based on the WHO histological grading system including conclusive information about isocitrate dehydrogenase 1 (IDH1) gene mutation status; (iv) patients subsequently treated according to standard of care, which included maximal safe and radical resection, radiotherapy, and concomitant and adjuvant chemotherapy with temozolomide.[3]

IDH1 mutation was routinely analyzed by immunohistochemical staining using an R132H point mutation specific

IDH1 antibody (Dianova). In cases in which IDH1 (R132H) immunohistochemical staining was not conclusive, both IDH1 and IDH2 mutation status were determined by pyrosequencing.

MRI Data Acquisition

MRI examinations (ie, phase 1 of the TME approach) were performed on a 3 Tesla clinical scanner (Tim Trio, Siemens) equipped with a standard 12-channel head coil. The MRI protocol included the following sequences: axial fluid attenuated inversion recovery (FLAIR; repetition time [TR]/echo time [TE]/inversion time [TI]: 5000/460/1800 ms; in-plane resolution: 0.45 × 0.45 mm, slice thickness: 3 mm); single-shot diffusion weighted echo planar imaging (DW-EPI) sequence (TR/TE: 5300/98 ms; in-plane resolution: 1.2 × 1.2 mm, slice thickness: 4 mm; 29 slices; parallel imaging using generalized autocalibrating partially parallel acquisition [GRAPPA] factor of 2, b-values of 0 and 1000 s/mm^2); and pre- and postcontrast enhanced T1-weighted gradient-echo MRI sequences (TR/TE: 250/2.8 ms; in-plane resolution: 0.5 × 0.5 mm, slice thickness: 4 mm; 29 slices).

For the quantitative blood oxygen level dependent (qBOLD) approach, we performed (i) a multi-echo gradient echo (GE) sequence for R_2*-mapping (8 echoes; TE, 5–40 ms) and (ii) a multi-echo spin echo (SE) sequence for R_2-mapping (8 echoes; TE, 13–104 ms), respectively.

For vascular architecture mapping (VAM), we used dynamic susceptibility contrast (DSC) perfusion MRI data obtained with SE (TR, 1740 ms; TE, 33 ms) and GE (TR, 1740 ms; TE, 22 ms) EPI sequences, respectively, in combination with a dual contrast agent injections approach.[15,16,19] Both DSC perfusion examinations were performed with 60 dynamic measurements and administration of 0.1 mmol/kg body weight gadoterate meglumine (Dotarem, Guerbet) at a rate of 4 mL/s using an MR-compatible injector (Spectris, Medrad) and with utmost caution for the injection time as described previously.[15,16] A 20-mL bolus of saline was injected subsequently at the same rate. Our strategies to minimize the probability of patient motions and differences in the time to first-pass peak, which may significantly affect the data evaluation, were described previously.[15,16] Geometric parameters were chosen identical for these 4 sequences: in-plane resolution: 1.8 × 1.8 mm, slice thickness: 4 mm; 29 slices; GRAPPA factor of 2. The additional acquisition time (TA) for the qBOLD (R_2* and R_2-mapping: TA, 1.5 and 3.5 min, respectively) and VAM sequences (SE-EPI DSC perfusion: TA, 2 min) was 7 minutes.

MRI Data Preprocessing and Calculation of MRI biomarker

Preprocessing of qBOLD and VAM data, and calculation of MRI biomarker maps for oxygen metabolism and neovascularization (phases 2 and 3 of the TME approach) were performed with custom-made MatLab (MathWorks) software. Both qBOLD and VAM preprocessing consisted of 3 steps.

qBOLD preprocessing: (i) corrections for background fields of the R_2*-mapping data[20] and for stimulated echoes of the R_2-mapping data,[21] (ii) calculation of R_2* and R_2 maps from the multi-echo relaxometry data, and (iii) calculation of absolute cerebral blood volume and flow maps from the GE-EPI DSC perfusion MRI data via automatic identification of arterial input functions.[22,23] These data were used for calculation of MRI biomarker maps of oxygen metabolism, including oxygen extraction fraction (OEF), cerebral metabolic rate of oxygen ($CMRO_2$),[17] and the average mitochondrial oxygen tension ($mitoPO_2$), respectively.[24,25]

VAM preprocessing: (i) correction for remaining contrast agent extravasation was performed as described previously,[15,26,27] (ii) fitting of the first bolus curves for each voxel of the GE- and SE-DSC perfusion data with a previously described gamma-variate function,[28] (iii) calculation of the $\Delta R_{2,GE}$ versus $(\Delta R_{2,SE})^{3/2}$ diagram[29]—the so-called vascular hysteresis loop. These data were used for calculation of MRI biomarker maps of neovascularization, including the microvessel type indicator (MTI) as well as the upper limit of microvessel radius (R_U) and microvessel density (N_U)[30] Supplementary Fig. S1 (phases 1–3) shows the procedure from MRI data acquisition over preprocessing to biomarker calculation schematically. The corresponding Supplementary text provides a more detailed discussion of the methodology.

Information Fusion and Tumor Microenvironment Classification

Fusion of MRI biomarker information about oxygen metabolism (OEF, $CMRO_2$, $mitoPO_2$) and neovascularization (MTI, R_U, N_U) as well as classification of TME (phase 4) were performed with custom-made MatLab software and consisted of 4 steps: (i) classification of the oxidative status in mitochondria; (ii) classification integrity of the tumor neovasculature; (iii) fusion of this classified information in one imaging dataset; and (iv) classification of TME within this dataset including and considering the $CMRO_2$-OEF scatterplot (see bottom of Supplementary Fig. S1 and the corresponding Supplementary text for a more detailed discussion). This procedure was associated with the introduction of 6 different TMEs for oxygen metabolism and neovascularization:

(i) A TME with $mitoPO_2$ < 10 mmHg (associated with high OEF and normal to high $CMRO_2$ compared with cNWM) and dysfunctional neovasculature was interpreted as hypoxia with defective tumor neovasculature ("Hypoxia, no neovascularization [NV]"; red voxels in the TME map).

(ii) A TME with $mitoPO_2$ < 10 mmHg (normal to low OEF and high $CMRO_2$) and functional neovasculature was interpreted as hypoxia with functional tumor neovasculature and predominantly mitochondrial oxidative phosphorylation for energy production ("Hypoxia + NV"; yellow voxels).

(iii) A TME with $mitoPO_2$ = 10–60 mmHg and no neovascularization (very high OEF and low $CMRO_2$) was interpreted as necrosis with highly defective vasculature ("Necrosis"; black voxels).

(iv) A TME with $mitoPO_2$ = 10–60 mmHg and neovascularization (low OEF and normal to high $CMRO_2$) was interpreted as normoxic tumor with functional tumor

neovasculature and, due to the high $CMRO_2$, predominantly mitochondrial oxidative phosphorylation for energy production ("OxPhos + NV"; green voxels).

(v) A TME with $mitoPO_2$ > 60 mmHg and neovascularization (very low OEF and low to normal $CMRO_2$) was interpreted as tumor tissue with high mitochondrial oxygen tension and functional neovasculature and, due to the low $CMRO_2$, predominantly glycolysis for energy production without mitochondrial involvement ("Glycolysis + NV"; blue voxels).

(vi) A TME with $mitoPO_2$ > 60 mmHg and no neovascularization (again very low OEF and low to normal $CMRO_2$) was interpreted as tumor tissue with high mitochondrial oxygen tension, without neovasculature, and due to the low $CMRO_2$, predominantly glycolysis for energy production without mitochondrial involvement ("Glycolysis, no NV"; blue voxels).

As described in parentheses above, the voxels of each TME were assigned different colors, which resulted in the so-called oxygen metabolism-neovascularization TME map. For higher clarity and better assessability of the TME maps, we decided to use blue color for both the "Glycolysis + NV" and the "Glycolysis, no NV" TME, resulting in 5 TMEs in the respective maps. This is additionally supported by the very small volume (≤5%) found for the "Glycolysis, no NV" TME.

Quantitative Analysis

For quantitative analysis of the TMEs, regions of interest (ROIs) were manually defined based on features seen in the FLAIR images for cNWM and in the contrast-enhanced T1-weighted images for the enhancing tumor region, respectively. The ROIs were transferred to the TME maps. The ROIs for enhancing tumor, which were transferred to the TME maps, covered at least 75% of the total tumor volume. The volumes of the 6 TMEs were calculated. The volume of the "Glycolysis + NV" TME was used for differentiation of phenotypes. MRI biomarker values for oxygen metabolism (OEF, $CMRO_2$, $mitoPO_2$) and for neovascularization (MTI, N_U, R_U) were averaged for each of the 6 TMEs and cNWM. Additionally, the total tumor volumes were calculated on contrast-enhanced T1-weighted MRIs.

Statistical and Survival Analysis

SPSS 21 software (IBM) was used for statistical evaluation. A Mann–Whitney test was used for comparison of volumes and biomarker values of the tumor subareas between the 2 phenotypes. Linear regression analyses were performed for correlations between MRI biomarkers for oxygen metabolism and neovascularization. *P*-values <0.05 were considered to indicate significance. We performed Kaplan–Meier survival analysis with the log-rank test on categorical clinical variables, including age ≥60 years, Karnofsky performance score (KPS) <80, extent of resection (EOR), and the discovered metabolic groups. EOR was determined by a postoperative MRI which was performed within 48 hours after surgery. Cross total resection was defined as complete resection (>95%) of the enhancing tumor, or else as subtotal resection (≤95%). Factors that were significant ($P < 0.05$) in univariate analysis were entered into multivariate survival analysis based on the Cox proportional hazard ratio (HR) model to assess the clinical significance of metabolic phenotypes in association with progression-free survival (PFS) after accounting for other clinical prognostic covariates. Progression was determined by at least 2 board-certified radiologists in consensus based on the updated Response Assessment in Neuro-Oncology criteria with clear radiological features of recurrence.[31] Overall survival (OS) was defined from the time of initial diagnosis to death. Patients without progression or still alive at last contact were censored for PFS or OS analysis, respectively.

Results

Patient Characteristics

A total of 57 consecutive patients fulfilled the study inclusion criteria. Five patients had a glioblastoma with a mutation of the IDH1 gene (IDH1mut). Due to the very small patient number, we decided to exclude these patients from the study. Finally, 52 patients (32 male; 63.5 ± 12.6 y; 36–86 y) with untreated glioblastomas with normal, wild-type gene (IDH1wt) were included for further evaluation. Nine patients had a KPS of 60–65, another 3 had a score of 70, and the rest had 80 or above. Median PFS was 173 days; 8 patients (15%) without progression at last contact were censored. Median OS was 224 days; 25 patients (48%) still alive at last contact were censored. Due to the high number of censored patients for OS, we decided to perform no further survival analysis for OS.

Intratumoral Heterogeneity of Oxygen Metabolism and Neovascularization

MRI biomarker maps of oxygen metabolism (OEF, $CMRO_2$, $mitoPO_2$) and neovascularization (MTI, N_U, R_U) were successfully calculated for all 52 patients suffering from glioblastoma IDH1wt. Both oxygen metabolism and neovascularization already provided indication for the spatial heterogeneity of TMEs within the lesion. Fig. 1 shows a representative example for the complex pattern of alterations in the MRI biomarker maps of oxygen metabolism and neovascularization (upper row) in a 61-year-old male glioblastoma patient. This made interpretation, even from a qualitative point of view, challenging and not straightforward. Information fusion (Fig. 1, lower row) of oxygen metabolism and neovascularization resulted in a single and more intuitive map (ie, the TME map). This map demonstrated the heterogeneity, spatial localization, size, and magnitude of physiologic features of the TMEs: necrosis, hypoxia, OxPhos, and glycolysis combined with/without neovascularization. The TME map as well as the $CMRO_2$-OEF scatterplot demonstrated that this glioblastoma was dominated by glycolysis (50.6% of the tumor volume) and functional, stable neovasculature with, however, low percentages of necrosis and hypoxia. In this patient, 80.8% of the tumor volume showed functional neovasculature and 19.2% defective neovasculature. Two further illustrative cases suffering from a glioblastoma with very

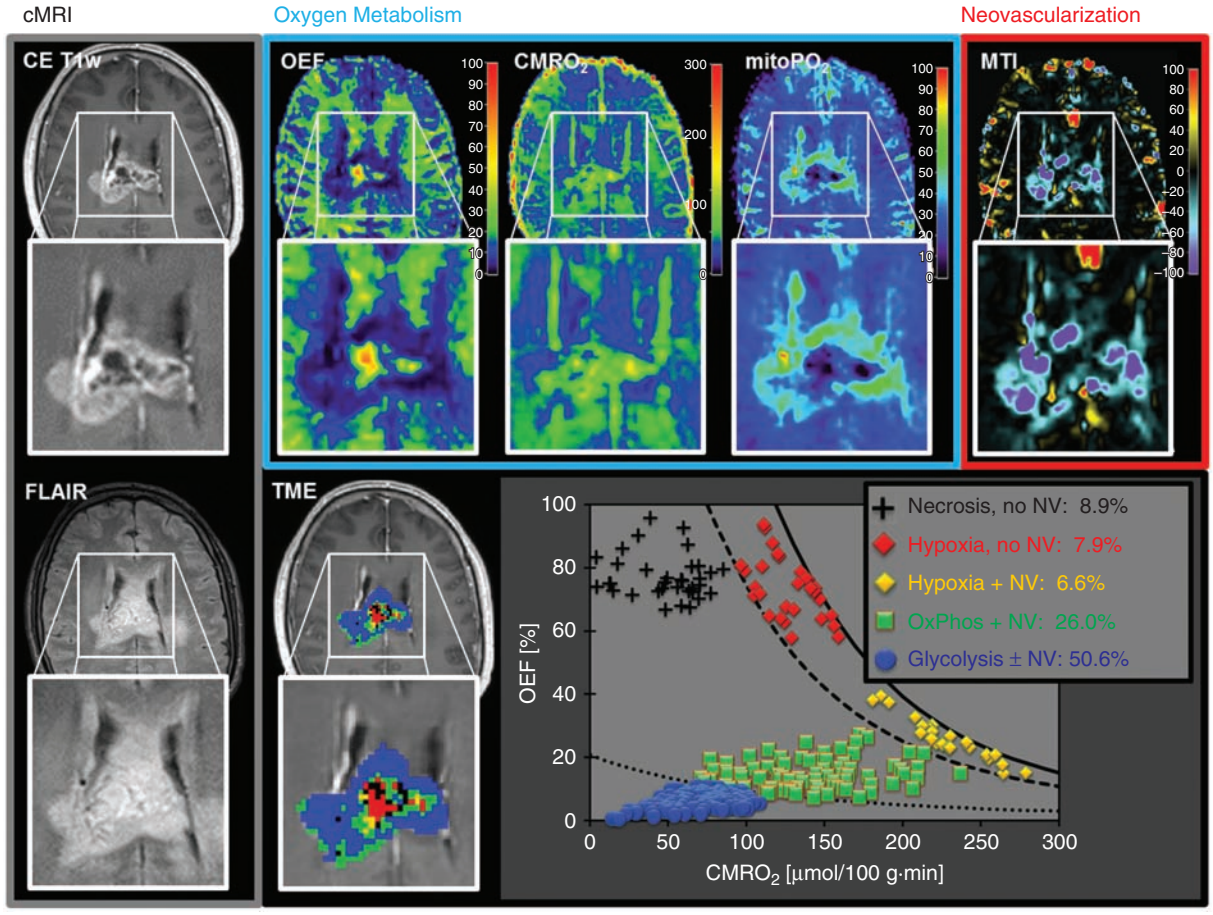

Fig. 1 Conventional anatomic MRI (cMRI; grey box), oxygen metabolism (OEF, $CMRO_2$, $mitoPO_2$; blue box), neovascularization (MTI; red box), and TME mapping (downright) in a 61-year-old male patient with glioblastoma IDH1wt. Oxygen metabolism and neovascularization demonstrated spatial heterogeneity within the lesion. Information fusion of oxygen metabolism and neovascularization using our TME approach resulted in the $CMRO_2$-OEF scatterplot and finally in the TME map. This glioblastoma was dominated by glycolysis (50.6% of the tumor volume) and functional, stable neovasculature (80.8% of the tumor volume showed neovascularization).

similar characteristics regarding heterogeneity of oxygen metabolism and neovascularization are presented in Supplementary Fig. S2.

Heterogeneity of alterations in the MRI biomarker maps of oxygen metabolism and neovascularization in the glioblastoma was similar in the patient presented in Fig. 2 (upper row). The TME map and the $CMRO_2$-OEF scatterplot, however, demonstrated that this glioblastoma was substantially less glycolytic (8.9% of the tumor volume), but more necrotic (21.5%) and especially more hypoxic (34.4% with no NV and 20.5% with NV, respectively) compared with the patients in Fig. 1 and Supplementary Fig. S2. In this patient, only 49.6% of the tumor volume showed functional neovasculature but 50.4% of the tumor vasculature was defective. Two other illustrative cases of glioblastoma with very similar characteristics are shown in Supplementary Fig. S3.

Although we detected differences in the percentage of the different TMEs related to the total tumor volume, the fundamental spatial structure and arrangement of the TMEs was similar in all patients: the central necrosis was surrounded by a hypoxic TME with defective vasculature followed by a hypoxic TME with (still) functional neovasculature. This necrotic/hypoxic tumor core, in turn, was surrounded by TMEs with predominantly mitochondrial OxPhos and glycolysis, respectively, for energy production.

Subgroups of Glioblastoma IDH1wt

Analysis of the "Glycolysis + NV" TME volumes for all 52 patients uncovered 2 subgroups of glioblastoma IDH1wt with no overlap for the range of these values. We used this parameter for differentiation of 2 phenotypes: (i) a glycolytic dominated phenotype with predominantly functional neovasculature; the range for the "Glycolysis + NV" TME volume was 33.9%–85.6% (53.8 ± 12.9%); (ii) a necrotic/hypoxic dominated phenotype with high percentage of defective tumor neovasculature; the "Glycolysis + NV" TME volume was 0.9%–18.0% (10.6 ± 5.0%; Fig. 3). All

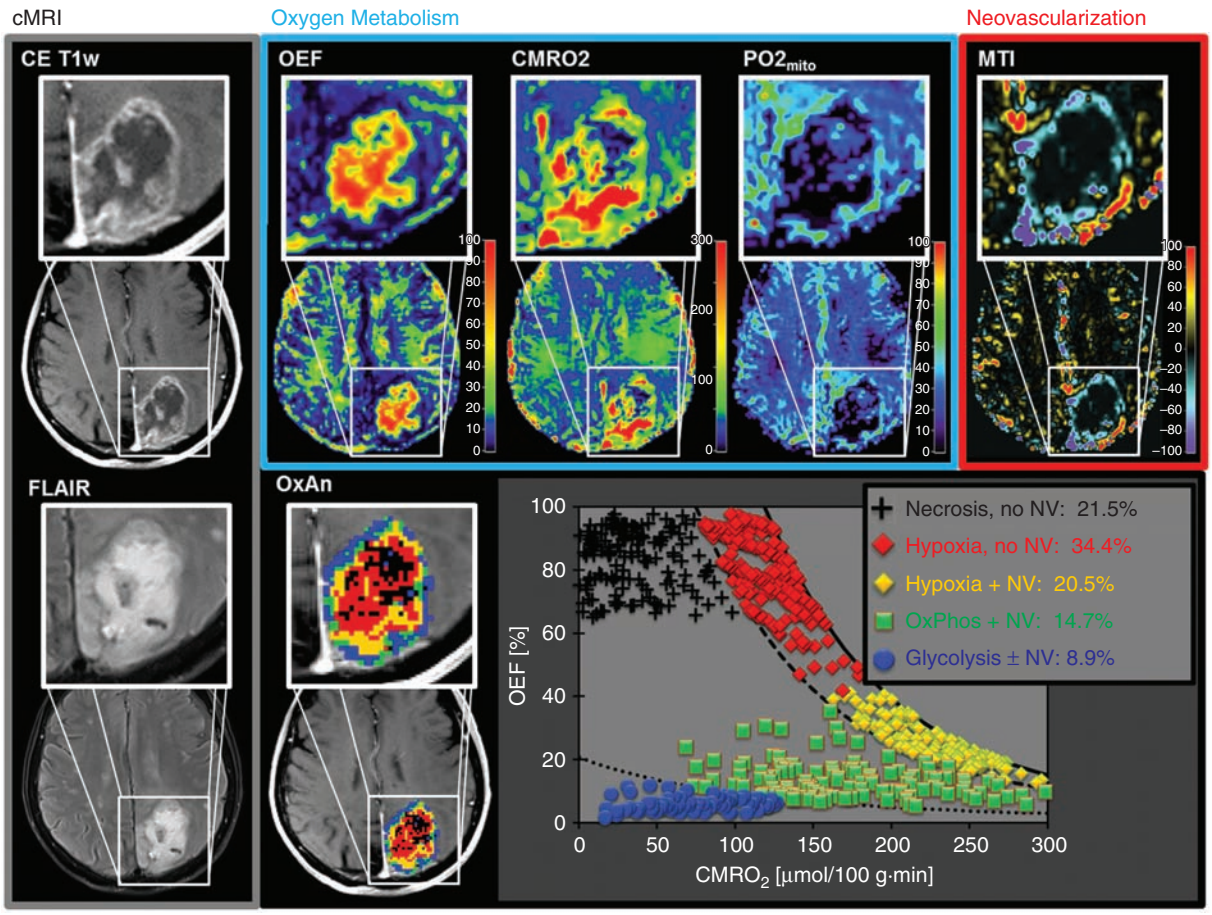

Fig. 2 Conventional anatomic MRI (cMRI; grey box), oxygen metabolism (OEF, $CMRO_2$, $mitoPO_2$; blue box), neovascularization (MTI; red box), and TME mapping (downright) in a 71-year-old female glioblastoma IDH1wt patient. Spatial heterogeneity of oxygen metabolism and neovascularization in this glioblastoma was similar to that in the patient in Fig. 1. The $CMRO_2$-OEF scatterplot, however, demonstrated a substantially lower percentage of glycolysis and higher percentage of necrosis (21.5%), hypoxia (total 54.9%), and defective tumor vasculature (50.4%).

other TME volumes (necrosis; hypoxia; and glycolysis, no NV) revealed an overlap of the ranges but significant differences between the 2 subgroups (all $P \leq 0.005$), except for the OxPhos (+NV) TME ($P = 0.978$), which revealed a very similar percentage: 19.6% versus 19.9%, respectively (Fig. 3). The very small percentage of the "Glycolysis, no NV" TME for both phenotypes (3.9% and 2.6%) supported our decision to use blue color for both glycolysis (with/without NV) TME to preserve clarity and assessability of the TME maps. Patient characteristics of the 2 subgroups of glioblastoma are presented in Supplementary Table S1. There were no significant differences in age, sex, KPS, contrast-enhanced T1-weighted MRI tumor volume, and EOR between the subgroups.

The mean $CMRO_2$ value averaged over the whole tumor volume was found significantly lower ($P < 0.001$) in the glycolytic compared with the necrotic/hypoxic phenotype. The percentage of tumor volume with functional neovasculature, however, was significantly larger ($P < 0.001$) in the glycolytic phenotype (Fig. 4A and B). Furthermore, we found a significant and strong correlation ($P < 0.001$, $R = 0.708$) between mean $CMRO_2$ and percentage of functional neovasculature in the necrotic/hypoxic subgroup, but not in the glycolytic subgroup ($P = 0.355$, $R = 0.185$; Fig. 4C). An overview of the biomarker values of oxygen metabolism and neovascularization for the different TMEs in the 2 phenotypes of glioblastoma IDH1wt is presented in Supplementary Table S2.

Survival Analysis

Kaplan–Meier survival analysis revealed that the glycolytic dominated phenotype with predominantly functional neovasculature showed significantly longer PFS (log-rank $P = 0.035$) compared with the necrotic/hypoxic dominated phenotype with high percentage of defective neovasculature (Fig. 4D). Univariate survival analysis in the entire cohort of patients showed that age at diagnosis (<60 y vs ≥60 y; $P = 0.423$) and sex (female vs male; $P = 0.593$) were not significant prognostic factors for PFS. These factors were not included in multivariate analysis. However, preoperative KPS (≥80 vs <80; $P = 0.007$; HR, 2.712), EOR

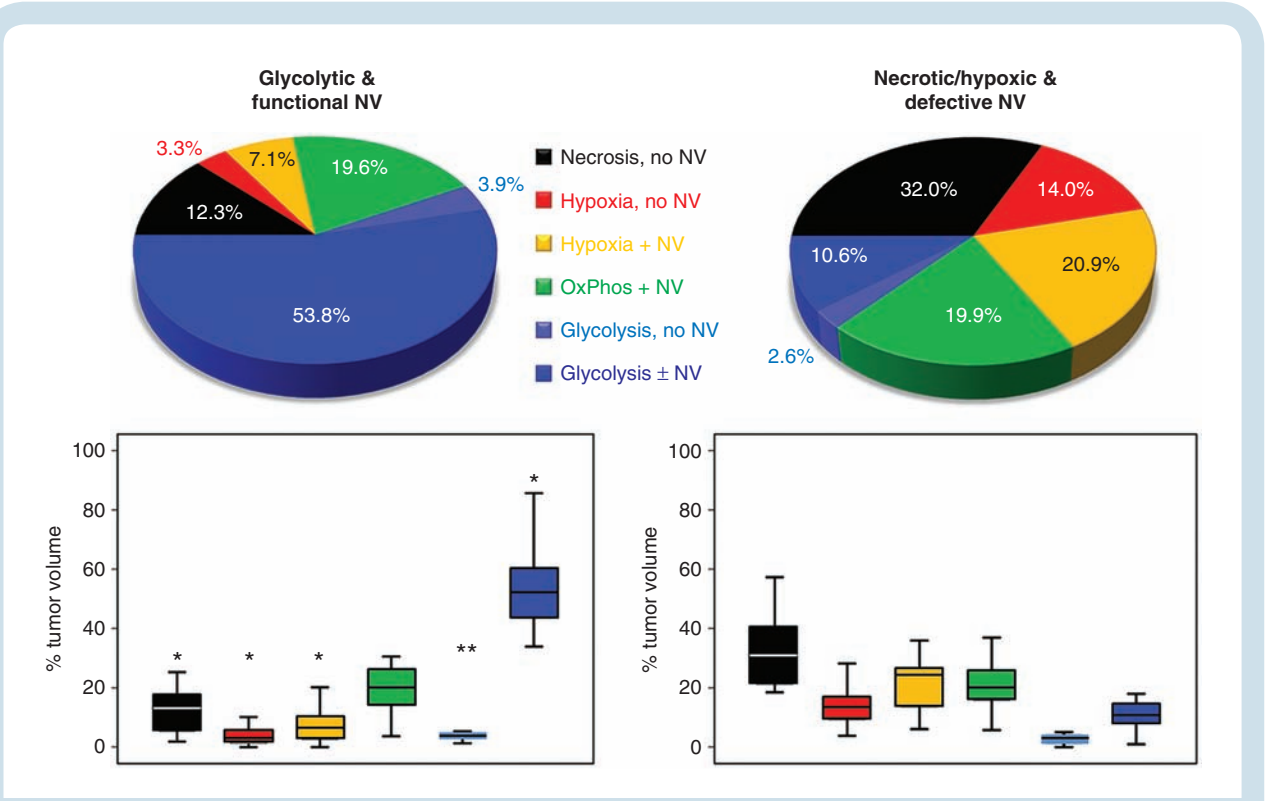

Fig. 3 Comparison of the 2 metabolic phenotypes of glioblastoma IDH1wt. Upper part: pie charts illustrating the percentage distribution of the TMEs for the glycolytic dominated phenotype with predominantly functional neovasculature (left) and the necrotic/hypoxic dominated phenotype with relatively high percentage of defective tumor neovasculature (right). Lower part: box and whisker plots show the percentage distribution of the TMEs. Boxes are mean ± SD, and whiskers are minimum and maximum values, respectively. Boxes marked with an asterisk (2 asterisks) in the glycolytic phenotype were significantly different from their counterparts in the necrotic/hypoxic phenotype (*$P < 0.001$; **$P = 0.005$).

(gross total vs subtotal resection; $P = 0.033$; HR, 2.269), and the metabolic phenotype (glycolytic vs necrotic/hypoxic; $P = 0.035$; HR, 1.920) were significant prognostic factors for PFS. For the multivariate analysis, however, age, preoperation, and metabolic phenotype lost significance as prognostic factors for PFS (Table 1).

Discussion

Heterogeneity of glioblastoma is of high relevance for both clinical patient management and research. In this study, we introduced an advanced imaging approach for non-invasive localization of hypoxic and vascular niches within the heterogeneously structured TME. After correlation of TME with the dominating metabolic strategy for energy production, we were able to identify 2 different metabolic phenotypes for newly diagnosed glioblastoma IDH1wt.

The finding of a common spatial structure and arrangement of the TMEs is conclusively explainable due to the known sequence of events during the development of glioblastoma obtained from preclinical studies and histopathology.[2,32] The widely accepted model of glioblastoma progression includes an explanation of the relationship between pseudopalisades, angiogenesis, and aggressive clinical behavior.[33,34] Initially, tumor cells infiltrate through the central nervous system and receive oxygen and nutrient supplies through vascular co-option of intact native blood vessels.[2] Co-opted vessels have been shown to express angiopoietin-2, which in the absence of vascular endothelial growth factor (VEGF) promotes endothelial cell apoptosis, vessel regression, vascular occlusion, and intravascular thrombosis within the tumor.[34] Tumor cells begin to migrate away from the increasing hypoxia around the vascular pathology and create a peripherally moving wave (known as pseudopalisades) and central necrosis. The zone of necrosis and hypoxia expands and the migrating hypoxic pseudopalisading glioma cells secrete hypoxia-inducible factor 1α and VEGF, leading to neovascularization and in further consequence to an accelerated outward expansion of tumor cells toward a new vasculature.

This model well explains the spatial structure and arrangement of the TMEs which we found in our study: a central necrosis was surrounded by hypoxia with defective vasculature and hypoxia with (still) functional neovasculature, respectively. This necrotic/hypoxic tumor core was enclosed by 2 TMEs with functional neovasculature: a rim with mitochondrial OxPhos followed by glycolysis, respectively. These rims represented the most active part of the glioblastoma, which showed, interestingly, mitochondrial OxPhos and glycolysis for energy production. This may

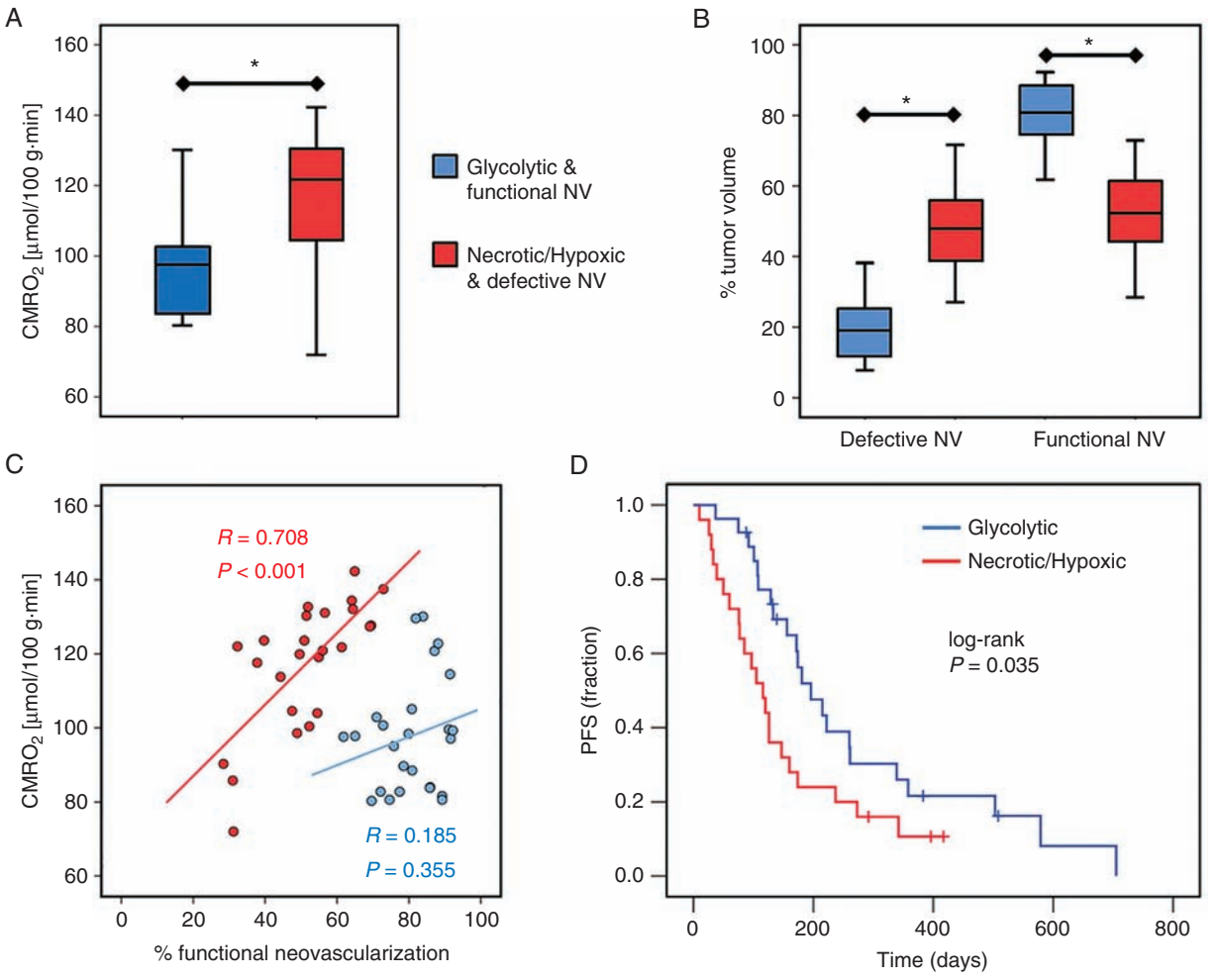

Fig. 4 Differences between the two metabolic phenotypes of glioblastoma IDH1wt and survival analysis. Box and whisker plots show (A) the mean $CMRO_2$ averaged over the whole tumor volume and (B) the percentage of tumor volume with defective and functional neovasculature, respectively. Boxes are mean ± SD, and whiskers are minimum and maximum values, respectively. Asterisks (*) mark significant differences between the 2 phenotypes ($P < 0.001$). (C) Scatterplot showing the correlation between mean $CMRO_2$ and percentage of tumor volume with functional neovasculature for the glycolytic (blue dots) and the necrotic/hypoxic phenotype (red dots). (D) Kaplan–Meier curves for PFS in the glycolytic (blue line) and the necrotic/hypoxic phenotype (red line).

Table 1 Univariate and multivariate analysis of PFS outcomes for glioblastoma patients with an IDH1wt tumor ($N = 52$)

	Univariate		Multivariate	
Characteristic	*P*-value	HR (95% CI)	*P*-value	HR (95% CI)
Age (≥60 y)	0.425	1.285 (0.694–2.380)		
Sex (male)	0.594	0.843 (0.449–1.582)		
Preop. KPS (<80)	0.009	2.712 (1.277–5.760)	0.145	1.808 (0.815–4.012)
EOR (subtotal)	0.038	2.269 (1.047–4.918)	0.077	2.077 (0.925–4.666)
Metab. PT (necr/hypox)	0.038	1.920 (1.036–3.560)	0.070	1.810 (0.952–3.440)

Abbreviations: Metab. PT (necr/hypox), metabolic phenotype (necrotic/hypoxic dominated phenotype with high ratio of defective neovascularization).

be explained as follows. It is well known that the necrotic/hypoxic tumor core is associated with host-mediated inflammatory response at the edge of the zone by activated macrophages and microglia.[35–38] Whether this response represents an active antitumor defense mechanism (M1) or a tumor-supportive one (M2) depends on the polarization of the microglia and macrophages. Wu et al[39] have shown that glioblastoma cancer stem cells can recruit and polarize microglia and macrophages to a tumor-supportive M2 phenotype, inhibiting phagocytosis, inducing secretion of immunosuppressive cytokines, and resulting in inhibition of T-cell proliferation. M2 polarization of microglia and macrophages, however, has been previously associated with oxidative phosphorylation.[40,41] Transferred to our findings, this may support the assumption that the outer hypoxic TME with functional neovasculature as well as the OxPhos TME—both showed the highest $CMRO_2$, which is characteristic for mitochondrial OxPhos—are regions with a high content of tumor-supportive microglia and macrophages recruited by the tumor to evade immune destruction and support cancer progression. The presence of the glycolytic TME can be explained as follows: proliferating cancer predominantly use aerobic glycolysis that ferments glucose into lactate, even in the presence of abundant oxygen. Glioblastoma cells use this metabolic shift toward aerobic glycolysis to generate precursors for anabolism to grow and generate enough ATP to maintain cell function.[42]

By analyzing the percentage of the different TMEs on the tumor volume, we uncovered 2 phenotypes of glioblastoma IDH1wt, which differ in the proportion of necrosis, hypoxia, neovascularization, and utilization of glycolysis for energy production. The glycolytic phenotype was associated with a stable functional neovasculature and a percentage of necrosis and hypoxia of less than 25% of the total tumor volume. This phenotype showed lower mean $CMRO_2$ and longer PFS compared with the necrotic/hypoxic phenotype. The necrotic/hypoxic phenotype was characterized by a high proportion of unstable defective dysfunctional neovasculature, suggesting a more aggressive tumor behavior. This phenotype had a strong linear correlation between mean $CMRO_2$ and percentage of functional neovasculature. This correlation is indicative of a coupling between oxygen metabolism and neovascularization and of a tumor vasculature which is incapable to sufficiently supply the tumor with oxygen.

With respect to tumor niches, the glycolytic phenotype with high percentage of stable functional neovasculature is dominated by the vascular niche. A close association between endothelial cells and neural stem cells was demonstrated in a seminal work by Shen et al.[43] They found that endothelial cells secrete factors that stimulate self-renewal of neural stem cells and proposed that endothelial cells are an integral component of the stem cell niche. This vascular niche has also been demonstrated in glioblastoma stem cells.[44,45] The vascular niche provides a protective microenvironment in which glioblastoma stem cells are able to freely proliferate and remain undifferentiated and are unaffected by any external influences.[44,45] In the necrotic/hypoxic phenotype with a high percentage of defective neovasculature, however, the hypoxic niche plays a major role, which is associated with tumor progression and resistance to both radiotherapy and chemotherapy.[2] Hypoxia promotes a more malignant phenotype of cancer cells and supports the survival of glioma stem cells, which possess greater drug resistance, self-renewal potential, and tumorigenicity.[46,47]

There are several limitations in our study. The number of patients for the subgroups ($N = 27$ vs 25) was relatively small and we were not able to include glioblastoma with mutation of the IDH1 gene as a separate subgroup. IDH1, however, is only mutated in ~10% of glioblastoma.[48] We were not able to provide valid data about OS due to the large number of censored patients in the survival analysis of OS. A further limitation of our study is that we did not include a validation of our approach. Biological validation of the MR-based parameters for $mitoPO_2$, $CMRO_2$, hypoxia, and neovascularization is required by correlation with findings from immunohistochemistry, invasive methods, or other imaging modalities (eg, PET).[49,50] Furthermore, we focused on the spatial heterogeneity within the gadolinium-enhanced tumor and excluded the peritumoral brain zone. In cases where the gadolinium-enhanced portion of the glioblastoma is completely resected, 90% of recurrences occur at the margin of surgical resection in the macroscopically normal peritumoral brain zone.[1] The purpose of our study, however, was to introduce a non-invasive imaging approach for localization and investigation of TME in glioblastoma.

In conclusion, we performed fusion of imaging parameters about energy production and neovascularization (2 hallmarks of cancer) and thereby gained a more precise insight into the intratumoral heterogeneity of human glioblastoma's pathophysiology. Our non-invasive mapping approach allows for user-independent classification of TMEs and detection of hypoxic and vascular niches in glioblastoma. This enabled us to identify patient subgroups with significantly different PFS. However, further studies are necessary including more patients, histopathologic correlation, peritumoral brain zone, and/or preclinical data for validation of the approach.

Supplementary Material

Supplementary material is available at *Neuro-Oncology* online.

Funding

This work was supported by the German Research Foundation (Deutsche Forschungsgemeinschaft, DFG; grant numbers STA 1331/3-1 and DO 721/9-1) and by the ELAN program (Erlanger Leistungsbezogene Anschubfinanzierung und Nachwuchsförderung; grant number 14-05-21-1-Stadlbauer).

Conflict of interest statement. The authors declare no potential conflicts of interest with respect to the research, authorship, and/or publication of this article.

References

1. Lemée JM, Clavreul A, Menei P. Intratumoral heterogeneity in glioblastoma: don't forget the peritumoral brain zone. *Neuro Oncol*. 2015;17(10):1322–1332.
2. Hardee ME, Zagzag D. Mechanisms of glioma-associated neovascularization. *Am J Pathol*. 2012;181(4):1126–1141.
3. Stupp R, Mason WP, van den Bent MJ, et al; European Organisation for Research and Treatment of Cancer Brain Tumor and Radiotherapy Groups; National Cancer Institute of Canada Clinical Trials Group. Radiotherapy plus concomitant and adjuvant temozolomide for glioblastoma. *N Engl J Med*. 2005;352(10):987–996.
4. Greaves M, Maley CC. Clonal evolution in cancer. *Nature*. 2012;481(7381):306–313.
5. Gillies RJ, Verduzco D, Gatenby RA. Evolutionary dynamics of carcinogenesis and why targeted therapy does not work. *Nat Rev Cancer*. 2012;12(7):487–493.
6. Marusyk A, Almendro V, Polyak K. Intra-tumour heterogeneity: a looking glass for cancer? *Nat Rev Cancer*. 2012;12(5):323–334.
7. Hambardzumyan D, Bergers G. Glioblastoma: defining tumor niches. *Trends Cancer*. 2015;1(4):252–265.
8. Quail DF, Joyce JA. The microenvironmental landscape of brain tumors. *Cancer Cell*. 2017;31(3):326–341.
9. Ho IAW, Shim WSN. Contribution of the microenvironmental niche to glioblastoma heterogeneity. *Biomed Res Int*. 2017;2017:9634172.
10. Lathia JD, Heddleston JM, Venere M, Rich JN. Deadly teamwork: neural cancer stem cells and the tumor microenvironment. *Cell Stem Cell*. 2011;8(5):482–485.
11. Cuddapah VA, Robel S, Watkins S, Sontheimer H. A neurocentric perspective on glioma invasion. *Nat Rev Neurosci*. 2014;15(7):455–465.
12. Vartanian A, Singh SK, Agnihotri S, et al. GBM's multifaceted landscape: highlighting regional and microenvironmental heterogeneity. *Neuro Oncol*. 2014;16(9):1167–1175.
13. Vander Heiden MG, Cantley LC, Thompson CB. Understanding the Warburg effect: the metabolic requirements of cell proliferation. *Science*. 2009;324(5930):1029–1033.
14. Stadlbauer A, Mouridsen K, Doerfler A, et al. Recurrence of glioblastoma is associated with elevated microvascular transit time heterogeneity and increased hypoxia. *J Cereb Blood Flow Metab*. 2018;38(3):422–432.
15. Stadlbauer A, Zimmermann M, Heinz G, et al. Magnetic resonance imaging biomarkers for clinical routine assessment of microvascular architecture in glioma. *J Cereb Blood Flow Metab*. 2017;37(2):632–643.
16. Stadlbauer A, Zimmermann M, Kitzwögerer M, et al. MR imaging-derived oxygen metabolism and neovascularization characterization for grading and IDH gene mutation detection of gliomas. *Radiology*. 2017;283(3):799–809.
17. Christen T, Schmiedeskamp H, Straka M, Bammer R, Zaharchuk G. Measuring brain oxygenation in humans using a multiparametric quantitative blood oxygenation level dependent MRI approach. *Magn Reson Med*. 2012;68(3):905–911.
18. Emblem KE, Mouridsen K, Bjornerud A, et al. Vessel architectural imaging identifies cancer patient responders to anti-angiogenic therapy. *Nat Med*. 2013;19(9):1178–1183.
19. Hsu YY, Yang WS, Lim KE, Liu HL. Vessel size imaging using dual contrast agent injections. *J Magn Reson Imaging*. 2009;30(5):1078–1084.
20. Preibisch C, Volz S, Anti S, Deichmann R. Exponential excitation pulses for improved water content mapping in the presence of background gradients. *Magn Reson Med*. 2008;60(4):908–916.
21. Prasloski T, Mädler B, Xiang QS, MacKay A, Jones C. Applications of stimulated echo correction to multicomponent T2 analysis. *Magn Reson Med*. 2012;67(6):1803–1814.
22. Bjørnerud A, Emblem KE. A fully automated method for quantitative cerebral hemodynamic analysis using DSC-MRI. *J Cereb Blood Flow Metab*. 2010;30(5):1066–1078.
23. Smith AM, Grandin CB, Duprez T, Mataigne F, Cosnard G. Whole brain quantitative CBF, CBV, and MTT measurements using MRI bolus tracking: implementation and application to data acquired from hyperacute stroke patients. *J Magn Reson Imaging*. 2000;12(3):400–410.
24. Gjedde A. Cerebral blood flow change in arterial hypoxemia is consistent with negligible oxygen tension in brain mitochondria. *Neuroimage*. 2002;17(4):1876–1881.
25. Vafaee MS, Vang K, Bergersen LH, Gjedde A. Oxygen consumption and blood flow coupling in human motor cortex during intense finger tapping: implication for a role of lactate. *J Cereb Blood Flow Metab*. 2012;32(10):1859–1868.
26. Boxerman JL, Schmainda KM, Weisskoff RM. Relative cerebral blood volume maps corrected for contrast agent extravasation significantly correlate with glioma tumor grade, whereas uncorrected maps do not. *AJNR Am J Neuroradiol*. 2006;27(4):859–867.
27. Boxerman JL, Prah DE, Paulson ES, Machan JT, Bedekar D, Schmainda KM. The Role of preload and leakage correction in gadolinium-based cerebral blood volume estimation determined by comparison with MION as a criterion standard. *AJNR Am J Neuroradiol*. 2012;33(6):1081–1087.
28. Ducreux D, Buvat I, Meder JF, et al. Perfusion-weighted MR imaging studies in brain hypervascular diseases: comparison of arterial input function extractions for perfusion measurement. *AJNR Am J Neuroradiol*. 2006;27(5):1059–1069.
29. Xu C, Kiselev VG, Möller HE, Fiebach JB. Dynamic hysteresis between gradient echo and spin echo attenuations in dynamic susceptibility contrast imaging. *Magn Reson Med*. 2013;69(4):981–991.
30. Jensen JH, Lu H, Inglese M. Microvessel density estimation in the human brain by means of dynamic contrast-enhanced echo-planar imaging. *Magn Reson Med*. 2006;56(5):1145–1150.
31. Weller M, Cloughesy T, Perry JR, Wick W. Standards of care for treatment of recurrent glioblastoma—are we there yet? *Neuro Oncol*. 2013;15(1):4–27.
32. Rong Y, Durden DL, Van Meir EG, Brat DJ. 'Pseudopalisading' necrosis in glioblastoma: a familiar morphologic feature that links vascular pathology, hypoxia, and angiogenesis. *J Neuropathol Exp Neurol*. 2006;65(6):529–539.
33. Brat DJ, Castellano-Sanchez A, Kaur B, Van Meir EG. Genetic and biologic progression in astrocytomas and their relation to angiogenic dysregulation. *Adv Anat Pathol*. 2002;9(1):24–36.
34. Holash J, Maisonpierre PC, Compton D, et al. Vessel cooption, regression, and growth in tumors mediated by angiopoietins and VEGF. *Science*. 1999;284(5422):1994–1998.
35. Noch E, Khalili K. Molecular mechanisms of necrosis in glioblastoma: the role of glutamate excitotoxicity. *Cancer Biol Ther*. 2009;8(19):1791–1797.
36. Zhang ZM, Yang Z, Zhang Z. Distribution and characterization of tumor-associated macrophages/microglia in rat C6 glioma. *Oncol Lett*. 2015;10(4):2442–2446.
37. Roggendorf W, Strupp S, Paulus W. Distribution and characterization of microglia/macrophages in human brain tumors. *Acta Neuropathol*. 1996;92(3):288–293.
38. Raza SM, Lang FF, Aggarwal BB, Fuller GN, Wildrick DM, Sawaya R. Necrosis and glioblastoma: a friend or a foe? A review and a hypothesis. *Neurosurgery*. 2002;51(1):2–12; discussion 12.
39. Wu A, Wei J, Kong LY, et al. Glioma cancer stem cells induce immunosuppressive macrophages/microglia. *Neuro Oncol*. 2010;12(11):1113–1125.
40. Derlindati E, Dei Cas A, Montanini B, et al. Transcriptomic analysis of human polarized macrophages: more than one role of alternative activation? *PLoS One*. 2015;10(3):e0119751.

41. O'Neill LA, Hardie DG. Metabolism of inflammation limited by AMPK and pseudo-starvation. *Nature*. 2013;493(7432):346–355.
42. Agnihotri S, Zadeh G. Metabolic reprogramming in glioblastoma: the influence of cancer metabolism on epigenetics and unanswered questions. *Neuro Oncol*. 2016;18(2):160–172.
43. Shen Q, Goderie SK, Jin L, et al. Endothelial cells stimulate self-renewal and expand neurogenesis of neural stem cells. *Science*. 2004;304(5675):1338–1340.
44. Calabrese C, Poppleton H, Kocak M, et al. A perivascular niche for brain tumor stem cells. *Cancer Cell*. 2007;11(1):69–82.
45. Gilbertson RJ, Rich JN. Making a tumour's bed: glioblastoma stem cells and the vascular niche. *Nat Rev Cancer*. 2007;7(10):733–736.
46. Bao S, Wu Q, McLendon RE, et al. Glioma stem cells promote radioresistance by preferential activation of the DNA damage response. *Nature*. 2006;444(7120):756–760.
47. Galli R, Binda E, Orfanelli U, et al. Isolation and characterization of tumorigenic, stem-like neural precursors from human glioblastoma. *Cancer Res*. 2004;64(19):7011–7021.
48. Parsons DW, Jones S, Zhang X, et al. An integrated genomic analysis of human glioblastoma multiforme. *Science*. 2008;321(5897):1807–1812.
49. Vajkoczy P, Schilling L, Ullrich A, Schmiedek P, Menger MD. Characterization of angiogenesis and microcirculation of high-grade glioma: an intravital multifluorescence microscopic approach in the athymic nude mouse. *J Cereb Blood Flow Metab*. 1998;18(5):510–520.
50. Valable S, Corroyer-Dulmont A, Chakhoyan A, et al. Imaging of brain oxygenation with magnetic resonance imaging: a validation with positron emission tomography in the healthy and tumoural brain. *J Cereb Blood Flow Metab*. 2017;37(7):2584–2597.